Nanoscale

PAPER

View Article Online
View Journal | View Issue

Cite this: *Nanoscale*, 2022, **14**, 15404

Visualisation of individual dopants in a conjugated polymer: sub-nanometre 3D spatial distribution and correlation with electrical properties†

Gustav Persson, [a] Emmy Järsvall, [b] Magnus Röding, [c,d] Renee Kroon, [b,e] Yadong Zhang, [f,g] Stephen Barlow, [f,g] Seth R. Marder, [f,g,h,i] Christian Müller [b] and Eva Olsson *[a]

While molecular doping is ubiquitous in all branches of organic electronics, little is known about the spatial distribution of dopants, especially at molecular length scales. Moreover, a homogeneous distribution is often assumed when simulating transport properties of these materials, even though the distribution is expected to be inhomogeneous. In this study, electron tomography is used to determine the position of individual molybdenum dithiolene complexes and their three-dimensional distribution in a semiconducting polymer at the sub-nanometre scale. A heterogeneous distribution is observed, the characteristics of which depend on the dopant concentration. At 5 mol% of the molybdenum dithiolene complex, the majority of the dopant species are present as isolated molecules or small clusters up to five molecules. At 20 mol% dopant concentration and higher, the dopant species form larger nanoclusters with elongated shapes. Even in case of these larger clusters, each individual dopant species is still in contact with the surrounding polymer. The electrical conductivity first strongly increases with dopant concentration and then slightly decreases for the most highly doped samples, even though no large aggregates can be observed. The decreased conductivity is instead attributed to the increased energetic disorder and lower probability of electron transfer that originates from the increased size and size variation in dopant clusters. This study highlights the importance of detailed information concerning the dopant spatial distribution at the sub-nanometre scale in three dimensions within the organic semiconductor host. The information acquired using electron tomography may facilitate more accurate simulations of charge transport in doped organic semiconductors.

Received 28th June 2022,
Accepted 29th September 2022

DOI: 10.1039/d2nr03554e

rsc.li/nanoscale

Introduction

Molecular doping allows the adjustment of the energy levels of organic semiconductors and tuning of the electrical conductivity by several orders of magnitude, which is crucial for enhancing the performance of organic electronic devices.[1] Advantageous aspects of organic semiconductors include cost-effective processing, light weight and mechanical flexibility;[2–4] although traditional organic electronic devices have historically underperformed their inorganic counterparts, considerable progress has been made in recent years and the performance of organic electronic devices, such as solar cells, light-emitting diodes and thermoelectric generators, is now approaching or surpassing that of their inorganic counterparts.[5–9] However, the ionisation and dissociation steps, as well as charge transport, are still not fully understood.[10] Knowledge of the position of individual dopants with respect to other dopants and the surrounding polymer is critical for developing a complete understanding of the doping process.[11]

[a]*Department of Physics, Chalmers University of Technology, 41296 Göteborg, Sweden. E-mail: eva.olsson@chalmers.se*
[b]*Department of Chemistry and Chemical Engineering, Chalmers University of Technology, 41296 Göteborg, Sweden*
[c]*RISE Research Institutes of Sweden, Biomaterials and Health, Agriculture and Food, 41276 Göteborg, Sweden*
[d]*Department of Mathematical Sciences, Chalmers University of Technology, 41296 Göteborg, Sweden*
[e]*Laboratory of Organic Electronics, Linköping University, 60174 Norrköping, Sweden*
[f]*School of Chemistry and Biochemistry and Center for Organic Photonics and Electronics, Georgia Institute of Technology, Atlanta, GA 30332-0400, USA*
[g]*Renewable and Sustainable Energy Institute, University of Colorado Boulder, Boulder, CO 80303, USA*
[h]*School of Chemical and Biological Engineering, University of Colorado Boulder, Boulder, CO 80303, USA*
[i]*School of Chemistry, University of Colorado Boulder, Boulder, CO 80303, USA*
† Electronic supplementary information (ESI) available. See DOI: https://doi.org/10.1039/d2nr03554e

It has been argued that the structural details of the fine-scale distribution of dopants, and of the dopant ions formed after electron transfer, affect the organic semiconductor performance.[12–18] At dopant concentrations of a few mol% the conductivity increases with the dopant concentration, often by several orders of magnitude. The relationship between dopant concentration and conductivity changes at higher concentrations where the conductivity increases less strongly and eventually the conductivity may start to decrease. It has been suggested that this decrease may be due to aggregation of the dopants, giving rise to a disruption of the organic semiconductor nanostructure.[19,20] There is, however, no direct evidence that such aggregates prevent dopants from being in molecular contact with the organic semiconductor since it is challenging to determine the spatial distribution of the dopants in the host matrix,[21] in part due to small dimensions of the molecules, which are commonly less than 1 nm^3.[22] Moreover, because of this lack of detailed knowledge, a homogeneous distribution of dopants is typically assumed in simulation models for electrical transport properties,[23] although a recent study has shown that incorporating experimental data relating to the detailed nanostructure of organic semiconductors can significantly improve the accuracy of such simulations.[24]

In this study we determine and visualise the position of individual dopant species of Mo(tfd-$COCF_3$)$_3$ within films of the semiconducting polymer p($g_4$2T–T) (oxidation potential $E_{on} \approx -0.44$ V *vs.* Fc/Fc^+; estimated ionisation energy IE = 4.7 eV, according to IE = 5.1 eV + E_{ox}; see Fig. 1 for chemical structures).[25,26] We chose to work with Mo(tfd-$COCF_3$)$_3$ since the dopant contains molybdenum,[25] which we expect to enhance contrast in electron microscopy images when embedded in the polymer matrix. The matrix polymer p($g_4$2T–T) was selected because it features excellent solubility in polar solvents, which facilitates coprocessing with the dopant. Moreover, Mo(tfd-$COCF_3$)$_3$ (E_{red} = +0.39 V *vs.* ferrocene/ferrocenium, $FeCp_2/FeCp_2^+$) readily oxidizes p($g_4$2T–T) (oxidation potential E_{red} = +0.39 V); indeed Mo(tfd-$COCF_3$)$_3$ monoanion can be further reduced to a dianion at −0.16 V, suggesting that transfer of two electrons from p($g_4$2T–T) to each dopant molecule is possible.[27]

The distribution of Mo(tfd-$COCF_3$)$_3$ is studied as a function of dopant concentration. The distance between dopant clusters is on the order of a few up to 10 nanometres. We have performed electron tomography with sub-nanometre resolution to quantitatively determine the spatial distribution of individual Mo(tfd-$COCF_3$)$_3$ species in three dimensions, paying attention to the position of the individual dopant species with respect to other dopant species and to the surrounding polymer. A gradual change in distribution is observed. Individual species and clusters of few dopants dominate at low concentrations. As the dopant concentration increases, the dopant species form larger clusters. It is important to note that even though the cluster size increases, each individual dopant species is still in close contact with the surrounding polymer due to the elongated morphology of the clusters. The structural observations are correlated with UV-Vis-NIR absorption spectroscopy and electrical measurements. The observed changes in dopant distribution and cluster morphology as well as ionisation efficiency, as a function of concentration, are consistent with the expected increase in energetic disorder with increasing dopant concentration.

Experimental

Materials

Previously reported procedures were used to prepare Mo(tfd-$COCF_3$)$_3$ [28] and p($g_4$2T–T)[29] (M_n = 24 kg mol^{-1}, PDI = 3.3). Special care was taken during synthesis of p($g_4$2T–T) to purify the material from any high *Z*-number elements such as Pd (see ESI† for further details). Poly(diallyldimethylammonium chloride) (PDADMAC, M_w = 400–500 kg mol^{-1}, 20 wt% in H_2O) and anhydrous acetonitrile (AcN, purity >99.8%) were purchased from Sigma Aldrich. Chloroform ($CHCl_3$, purity >99.8%) was obtained from Fisher Scientific. All commercial solvents were used as received without further purification.

Sample preparation

Thin films were prepared by co-processing p($g_4$2T–T) and Mo(tfd-$COCF_3$)$_3$. Stock solutions were prepared by dissolving p($g_4$2T–T) and Mo(tfd-$COCF_3$)$_3$ in AcN : $CHCl_3$ (1 : 1, v : v) at concentrations of 10 g L^{-1} and 4 g L^{-1}, respectively. The solutions were mixed by adding appropriate volumes of AcN : $CHCl_3$ (1 : 1, v : v) to the p($g_4$2T–T) solutions before addition of the Mo(tfd-$COCF_3$)$_3$ solution to maintain a polymer concentration of 1 g L^{-1} (TEM) and 3 g L^{-1} (optical spectroscopy) in each polymer : dopant solution, while varying

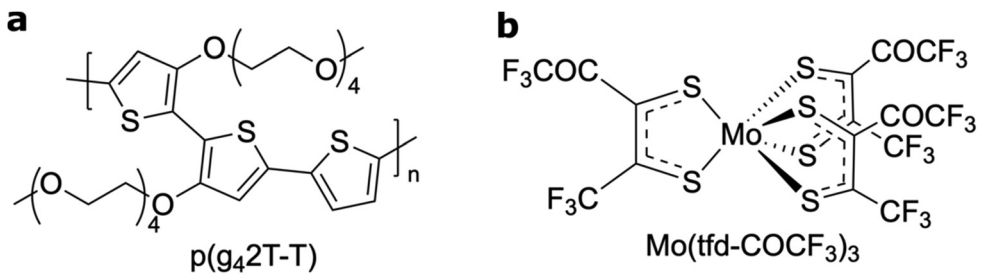

Fig. 1 Molecular structures of (a) the polymer p($g_4$2T–T) and (b) the molecular dopant Mo(tfd-$COCF_3$)$_3$.

the concentration of Mo(tfd-$COCF_3$)$_3$. The dopant concentration in mol% is calculated based on the molar mass of the polymer repeat unit and the molar mass of the dopant.

Samples for TEM analysis were prepared by spin casting (1000 rpm, 500 rpm s^{-1}, 40 s) an initial layer of PDADMAC (diluted to 1 wt% in MiliQ H_2O) onto microscopy glass slides, followed by spin casting of the polymer : dopant solution. This yielded a polymer : dopant film thickness of 10–20 nm. The TEM samples were immersed in MilliQ water resulting in the dissolution of the PDADMAC layer and the p($g_4$2T–T) : Mo(tfd-$COCF_3$)$_3$ films subsequently floated to the surface. 400 Cu mesh TEM grids (TED Pella) were used to extract the films. To ensure complete solvent evaporation, the films were stored in a dry and dark environment.

Thin films for optical- and electrical characterisation were prepared by spin casting p($g_4$2T–T) : Mo(tfd-$COCF_3$)$_3$ solutions onto microscopy glass slides, yielding a film thickness of 40–90 nm.

All samples for TEM analysis, optical- and electrical characterisation were prepared at the same time to minimise sample batch-to-batch variations.

Scanning transmission electron microscopy

Analysis using scanning transmission electron microscopy (STEM) was performed with a FEI Titan 80–300 TEM, with a corrector for spherical aberration of the condenser lens system, using an acceleration voltage of 300 kV. The high-angle annular dark field (HAADF) signal was used to form the images. Elemental analysis using energy dispersive X-ray spectroscopy (EDX) was performed with an Oxford X-sight spectrometer attached to the microscope.

Tomography reconstructions and analysis

Tilt series for electron tomography were acquired with the software Xplore 3D (FEI Company). The tilt series used a Saxton scheme spanning angles of ±70° with a tilt step varying from 0.9° to 2.5°, for a total of 79 images per tilt series.[30] Reconstructions were done using the software IMOD (University of Colorado).[31] The series were aligned using cross-correlation, and the simultaneous iterative reconstruction tomography (SIRT) algorithm (run for 25 iterations) was used to reconstruct the volumes. The final reconstructions were visualised using the software Visualizer-evo (System In Frontier Inc.). 3D meshes representing the dopant clusters were created by applying intensity thresholds on the reconstructions. The threshold values for each sample were optimised relative to each other by keeping a ratio of 5 : 20 : 40 dopant voxels for the samples with concentrations of 5 mol%, 20 mol% and 40 mol% Mo(tfd-$COCF_3$)$_3$. A red colour in the volumes was chosen to represent the position of the dopant molecule and a slightly lower intensity threshold was added as a semi-transparent yellow colour to the figures to represent potential wobble of dopant fluorinated pendant groups during acquisition of the tilt series. The positions of individual dopant species were fit to data by adding correctly sized markers to the reconstructions.

Quantitative image analysis

The reconstructed volumes of the samples with Mo(tfd-$COCF_3$)$_3$ concentrations of 5 mol%, 20 mol%, and 40 mol% were all cropped to an in-plane size of 150 nm × 150 nm. The thickness of each cropped volume was selected independently for each sample, based on an estimate of the film thickness from the image data. The image data were segmented (separating clusters and background) by Gaussian smoothing (σ = 0.5 voxels) and intensity thresholding, followed by another Gaussian smoothing (σ = 0.5 voxels) and a final intensity thresholding. The threshold values were selected to ensure that the number of voxels identified as dopant clusters adhered to the ratio of 5 to 20 to 40 between the different samples to accurately reflect the relative amount of dopant. The second iteration of smoothing and intensity thresholding helped to reduce noise in the segmentation.

Individual clusters were identified, keeping only the clusters with 3 voxels (approximately the volume of a single molecule) or more. Three different characteristics were computed from the clusters: volume, aspect ratio, and nearest-neighbour distance. The volume was computed in a straightforward manner from the volume of a single voxel. The aspect ratio was computed by approximating the cluster with an ellipsoid having the same second moments as the cluster itself, defining the aspect ratio as the ratio of the major and the minor axes. The nearest-neighbour distance is simply the Euclidean distance to the nearest cluster based on centroid coordinates. To account for the finite size of the volume, mirror boundary conditions were used in the latter case. The analysis was implemented using the software Matlab (MathWorks).

UV-Vis-NIR absorption spectroscopy

Measurements were performed with a PerkinElmer Lambda 1050 spectrometer.

Electrical characterisation

The electrical resistivity was measured with a four-point probe setup from Jandel Engineering (cylindrical probe head, RM3000) using collinear tungsten carbide electrodes with equidistant spacing of 1 mm that were held down with a constant weight of 60 g. The electrical conductivity (σ) was then calculated according to $\sigma = ((V/I)kt)^{-1}$ where V is the voltage, I is the current, k = 4.53 is a geometrical correction factor and t is the thickness.

Results and discussion

Structural analysis

Initial HAADF-STEM experiments yielded overview images of how the doped polymer thin-film structure varies as a function of composition (Fig. 2a–c). All images show bright areas on a darker continuous background. The HAADF-STEM imaging technique provides atomic number contrast (Z-contrast), where the intensity increases with the atomic number (Z-number).[32] The bright areas in Fig. 2a–c thus correspond to regions with higher Z-number. The average Z-number of the

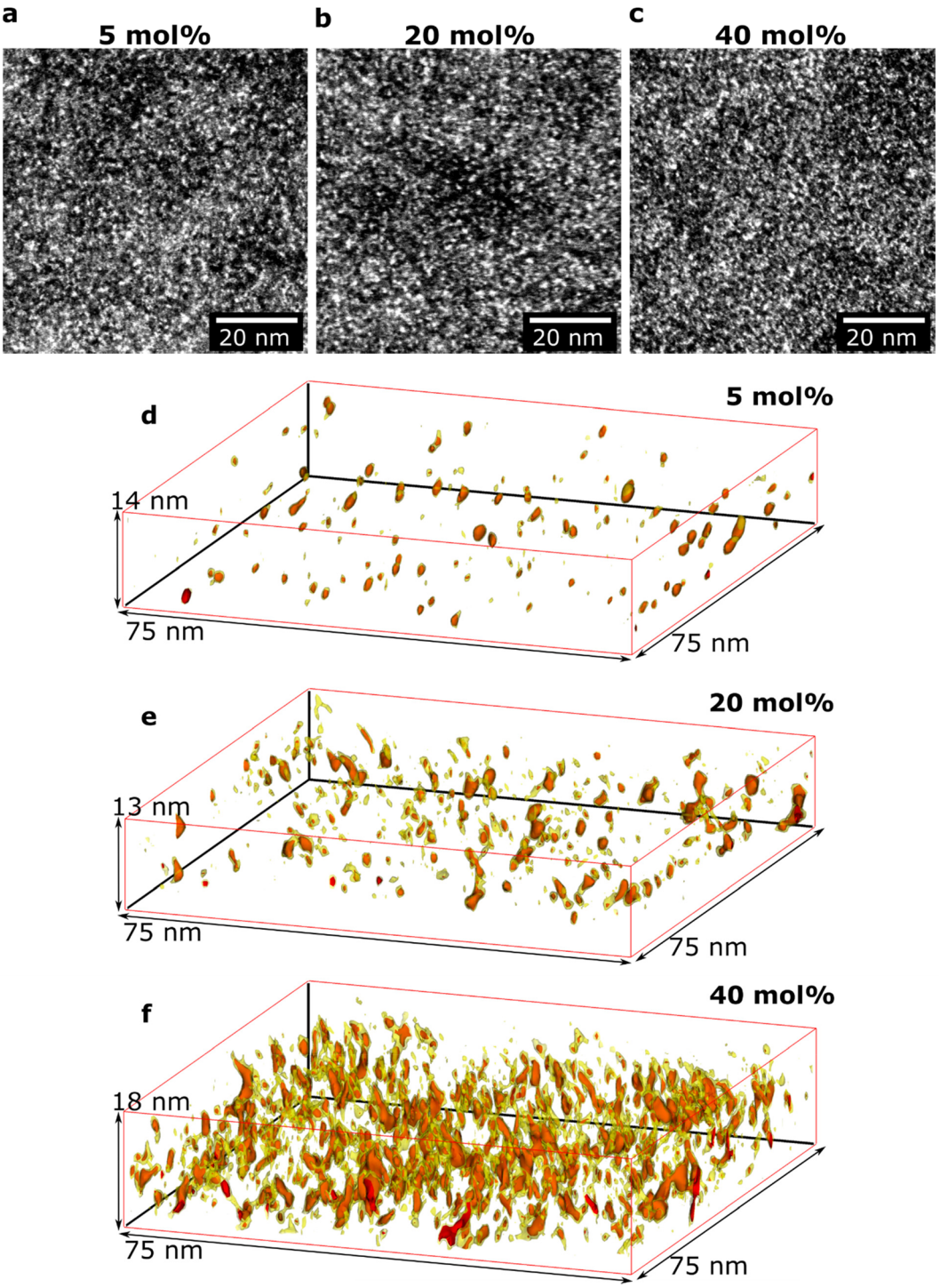

Fig. 2 Electron microscopy (a–c) HAADF-STEM images of representative areas and (d–f) tomography reconstructions of p($g_4$2T–T) doped with 5, 20, and 40 mol% Mo(tfd-$COCF_3$)$_3$, respectively. The sizes of the volumes are marked in nm. Red intensity thresholds in the reconstructions were chosen in order to visualise the position of Mo(tfd-$COCF_3$)$_3$ species. A lower intensity threshold is displayed in yellow.

dopant Mo(tfd-$COCF_3$)$_3$ is 20.0 while the corresponding *Z*-number of the surrounding polymer p($g_4$2T–T) is 7.7; the brighter areas, therefore, show the position of Mo(tfd-$COCF_3$)$_3$ species. Elemental analysis using EDX confirmed that the only high *Z*-number element present in the samples is Mo, and that the relative Mo signal increased for samples with higher dopant concentration (Fig. S1†). The appearance of the film structures is similar for all studied samples in these two-dimensional projection images, showing a relatively even distribution of the bright areas in the polymer.

In another set of experiments, the 3D structures of the films, including the size and the 3D morphology of the individual dopant regions, were determined. Electron tomography was performed for three different dopant levels (see Fig. 2d–f). Care was taken to obtain sufficient spatial resolution in the 3D reconstructions to resolve individual dopant species in the films. A voxel size of 0.5 nm was chosen for all reconstructions, which is smaller than the size of one dopant molecule (*ca.* 1.2 nm along the long axis and 0.6 nm along the short axis).[25] The red intensity areas in Fig. 2d–f represent the positions of dopant molecules. The yellow colour represents a slightly lower intensity value. Regions showing the yellow intensity interval are seen surrounding the dopant volumes with red intensity. The yellow regions can be interpreted to correspond to the fluorinated pendant groups due to their higher *Z*-number compared to the surrounding p($g_4$2T–T), and likely conformational changes during the acquisition of the tilt series giving rise to a slight smearing of the regions. Videos of rotating reconstructed volumes are included in ESI Videos S1–3† where inspection from all angles is provided. For each sample, a volume equivalent to an in-plane area of 2600 μm^2 is reconstructed and analysed to ensure that the observations are representative of the films. A significant difference in nanostructure of the three films is evident in the 3D reconstructions. The data show the presence of both isolated individual dopant species (molecules, or molecular mono- or dianions) as well as clusters of dopant species. The size of the clusters increases with increasing dopant level. In addition, the distance between the clusters decreases with increasing dopant level (see Table 1).

We observe that some dopant species are individually dispersed in the polymer matrix while others form clusters (Fig. 3a–c). Based on the information of the distribution of individual Mo(tfd-$COCF_3$)$_3$ species obtained from the tomography reconstructions, markers were used to visualise the 3D position of each Mo(tfd-$COCF_3$)$_3$ species in the sub-volumes (Fig. 3d–f). The markers in the figures are spherical with diameters corresponding to the largest dimension of the dopant molecule. The size of the dopant clusters increases with dopant concentration. In case of the film containing 5 mol% Mo(tfd-$COCF_3$)$_3$ the dopant species are present either as isolated species or in clusters of only a few species. The clusters start to form elongated chains as the concentration increases.

The average number of Mo(tfd-$COCF_3$)$_3$ species per cluster was determined by analysing the size distributions of 50 clusters in each sample (ESI Fig. S2†), resulting in values of 3.4, 4.6, and 11 species for dopant concentrations of 5 mol%, 20 mol%, and 40 mol%, respectively (see Table 1). This is a quantitative confirmation of the visual impression of the effect of concentration on the cluster size distribution obtained from the data in Fig. 3. The next step was to further refine the statistical analysis. An analysis was performed using the Matlab software procedure described in the Experimental section. The average cluster volumes were estimated to be 1.7 nm^3, 3.0 nm^3, and 3.1 nm^3 for the specimens, further confirming the gradual increase in cluster volume with increasing dopant concentration. Histograms of the distribution of cluster volumes at different dopant concentrations show that besides larger average volumes, anomalous larger clusters sizes appeared at high dopant concentrations with a few clusters having volumes of up to 15 nm^3 (Fig. 4a).

In addition to the trend of increasing cluster volume, the reconstructions show a change in cluster morphology. At 5 mol%, typical clusters have a round shape. This appearance changes to an increasingly elongated shape at higher dopant levels, with a preference for out-of-plane orientation of the long axis. This structural change was quantified by measuring the aspect ratios of the clusters (Fig. 4b). The distribution of aspect ratios features multiple peaks, especially for 20 and 40 mol% Mo(tfd-$COCF_3$)$_3$, indicating that some conformations of dopant clusters may be more frequent compared to others. The average cluster aspect ratio for 5 mol% is 2.1, which is close to the aspect ratio of single dopant species. A general trend of higher average aspect ratio and wider aspect-ratio distribution are evident for the higher dopant concentrations, *i.e.* 20 mol% and 40 mol%, compared to 5 mol%. This is consistent with the elongated shapes visible in the reconstructions (Fig. 2d–f). Clusters that are elongated in the out-of-plane direction have been reported before by Donhauser *et al.*,[33] who visualised co-evaporated composites of the organic compound 4,4′-bis(*N*-carbazolyl)-1,1′-biphenyl (CBP) and MoO_3. It is interesting to note that doping of CBP with MoO_3 was performed using co-evaporation, while in the present study p($g_4$2T–T) and Mo(tfd-$COCF_3$)$_3$ were co-processed from a mixed solution. Evidently, elongated clusters of dopant species can form in both polymer and small molecule hosts processed using different techniques.

Due to the lack of information about the distribution of dopants in the semiconductor host, models for the prediction of charge transport most often assume that the dopant distri-

Table 1 Quantitative information from data analysis of tomography reconstruction of films doped with different molar percentages of Mo(tfd-$COCF_3$)$_3$ (mol% of dopant relative to the polymer repeat unit) regarding cluster volume, elongation ratio and distance to closest neighbouring cluster. Average values with 95% confidence intervals are provided. The dopant–dopant distance of a hypothetical homogeneous sample is provided as a comparison

Mo(tfd-$COCF_3$)$_3$ (mol%)	5	20	40
Avg. volume per cluster (nm^3)	1.71 ± 0.17	2.96 ± 0.38	3.11 ± 0.24
Avg. aspect ratio	2.14 ± 0.06	2.40 ± 0.06	3.02 ± 0.06
Avg. nearest-neighbour distance (nm)	5.17 ± 0.22	3.53 ± 0.10	3.03 ± 0.05
Homogeneous dopant distance (nm)	2.75	1.63	1.18

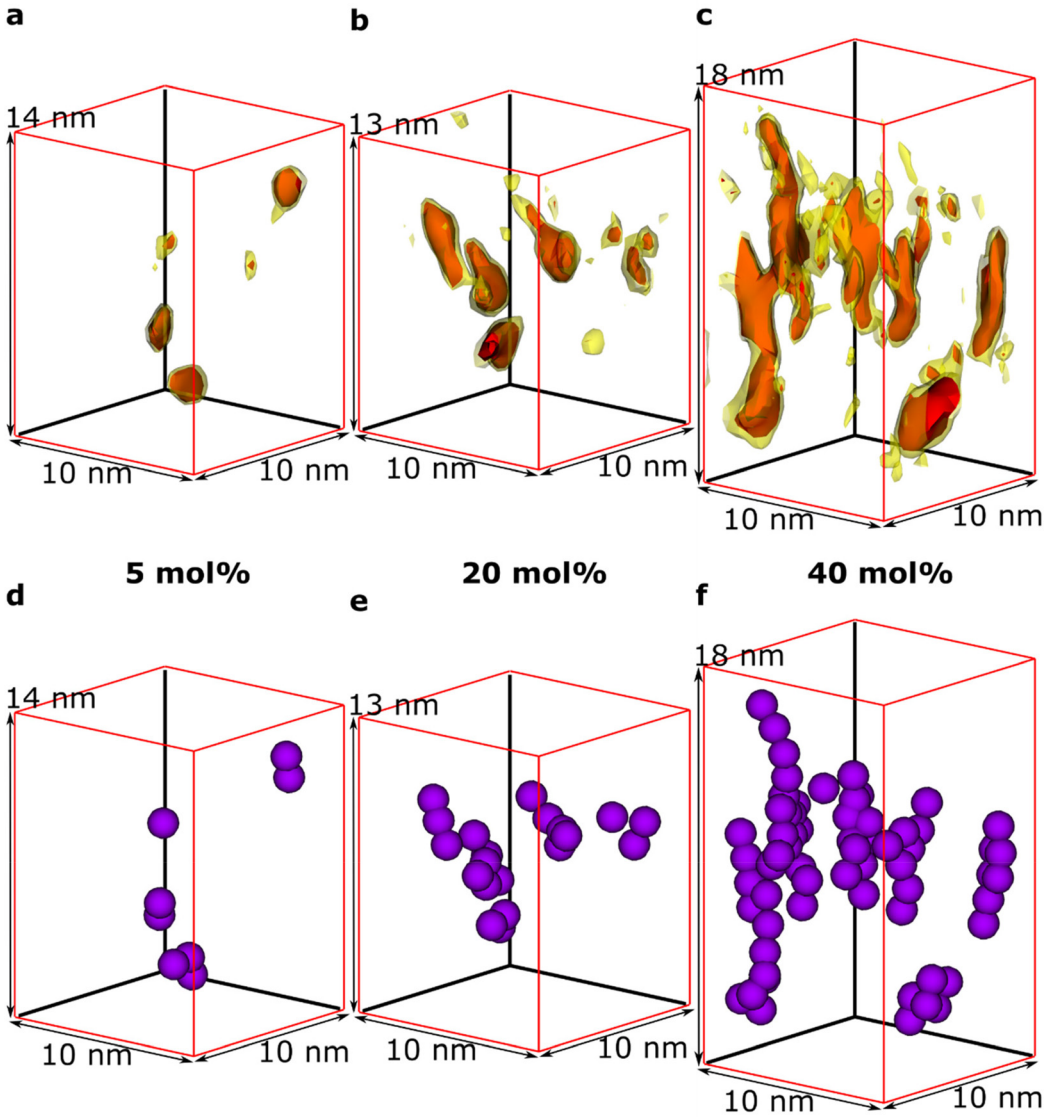

Fig. 3 Representative sub-volumes of the tomographic reconstructions of p($g_4$2T–T) doped with 5, 20, and 40 mol% Mo(tfd-$COCF_3$)$_3$, respectively. (a–c) Reconstructed sub-volumes showing the clusters and (d–f) markers indicate the positions of individual Mo(tfd-$COCF_3$)$_3$ species in the clusters and visualise the gradual change in cluster morphology.

bution is homogeneous. This is in distinct contrast to our experimental observations. The visualisation of the 3D film structure shows both a size distribution of the dopant clusters and also that the cluster morphology changes with dopant concentration. As a consequence, the distance between the clusters does not show a linear dependence on concentration (see Fig. 4c). The histograms of the distribution of distances to the nearest neighbour cluster in the samples show a wider distribution of distances for the sample containing 5 mol% dopant. The distribution is narrower for higher dopant concentrations. The average distance to neighbouring clusters is 5.8 nm for 5 mol%, 3.9 nm for 20 mol%, and 3.3 nm for 40 mol% Mo(tfd-$COCF_3$)$_3$. These numbers are significantly different from the estimated distances between dopant species in hypothetical homogeneous samples, *i.e.* 2.8, 1.7 and 1.2 nm, respectively. The experimental analysis of the position of dopant species provides information that can be expected to facilitate more accurate modeling of charge transport in doped semiconductor films.

It should be noted that although the dopant cluster size increases with dopant concentration, the elongated morphology of the clusters nevertheless allows each dopant species to be in contact with the surrounding organic semiconductor matrix (see Fig. 3d–f). Therefore, the ionisation efficiency of the dopant species can be expected to be higher compared to the case of a more spherical cluster morphology.[34] These observations are consistent with results from films of a benzodithiophene-thieno thiophene copolymer

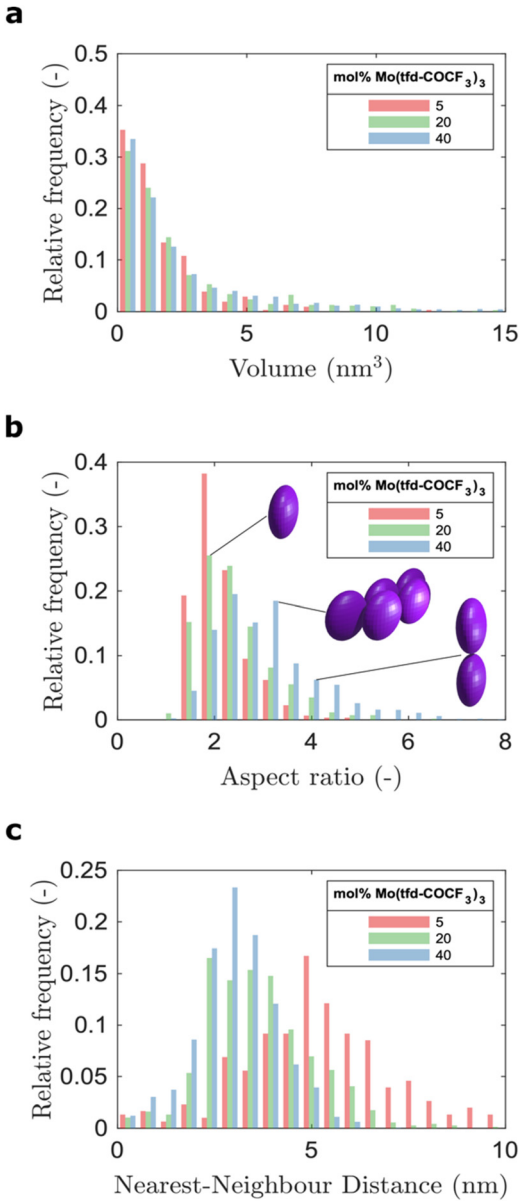

Fig. 4 Histograms from data analysis including all clusters in a volume equivalent to an in-plane area of 150 nm by 150 nm for each sample, displaying distribution of (a) cluster volume, (b) cluster aspect ratio and (c) nearest-neighbour cluster distance. Examples of dopant cluster conformations for different aspect ratios are illustrated as insets in (b).

doped with Mo(tfd-COCF$_3$)$_3$, where a detailed NMR study revealed that dopant clusters that were several tens of nm in size still did not contain unreacted dopants. However, this was not confirmed by imaging because the individual dopant species could not be resolved.[19]

Optical and electrical analysis

UV-Vis-NIR spectroscopy of doped films reveals the emergence of pronounced polaronic absorption bands at 900 nm and in the near infrared, confirming that electron transfer occurs (Fig. 5a). The evolution of the UV-vis-NIR absorbance spectra with dopant concentration is consistent with a gradual increase in polaron density and indicates that for 5–20 mol% Mo(tfd-COCF$_3$)$_3$ mostly polarons are present, while for 30 and 40 mol% both polarons and polaron pairs exist.[35] This is in agreement with our electron tomography analysis, which indicates that the dopants remain in contact with the surrounding polymer matrix and are not spatially prevented from engaging in electron-transfer reactions with the polymer, despite clustering. The polaron density of samples doped with 5–20 mol% Mo(tfd-COCF$_3$)$_3$ was estimated using a value for the molar attenuation coefficient of $\varepsilon = (4.1 \pm 0.2) \times 10^3$ m^2 mol^{-1} at 800 nm, which we have previously determined for electrochemically oxidized poly(3-hexylthiophene) (P3HT).[36] We compared ε with the thickness-normalized absorbance of doped p(g$_4$2T–T) films, as described previously,[35] and obtained a polaron density of 1–3 × 10^{26} m^{-3}, which corresponds to an ionization efficiency of around 200% for films containing 5 and 10 mol% dopant (*i.e.* the dopant species present are essentially all dianions), while samples doped with 20 mol% Mo(tfd-COCF$_3$)$_3$ featured an ionization efficiency of 118% (Table S1†). These estimates indicate that the ionization efficiency decreases with dopant concentration.

For 5–20 mol% Mo(tfd-COCF$_3$)$_3$, there is a steep increase in electrical conductivity as a function of dopant concentration (Fig. 5b). For 20–30 mol% Mo(tfd-COCF$_3$)$_3$ only a slight further increase in electrical conductivity is observed and for 40 mol% a lower value was measured. As discussed earlier, this conductivity trend as a function of dopant concentration has been observed in previous studies for other dopant–organic semiconductor combinations and has been attributed to a disruption of the nanostructure at high dopant concentrations.[19,20] Interestingly, the conductivity trend changes at approximately the same concentrations where changes in cluster shape and size were observed in the tomography reconstructions. However, the analysis of the nanostructure reveals that there are no large dopant aggregates present in any of the samples. Hence, each one of the dopant species should still be in proximity to the polymer and be able to undergo electron transfer, at least from a steric point of view.

It has been noted in a recent study that clustering of dopant species can have a direct impact on the electrical properties of organic semiconductors.[37] Through modeling, the authors showed that an increase in the number of dopants in clusters from 1 to 6 species leads to a widening of the density of states (DOS). A wider DOS indicates that the dopant clustering increases the energetic disorder in the system, and this in turn can negatively affect the conductivity. As the clusters observed in the current study may be larger than 6 species and, more notably, there are large variations in dopant cluster size, we expect that the energetic disorder increases with the concentration of Mo(tfd-COCF$_3$)$_3$. Another recent study suggests that a drop in dopant ionisation efficiency at high dopant concentrations may occur partially or completely due to a low entropy effect, and does not require large aggregated dopant phases.[38] At high dopant concentrations, the number of neighbouring dopant molecules will increase at the expense

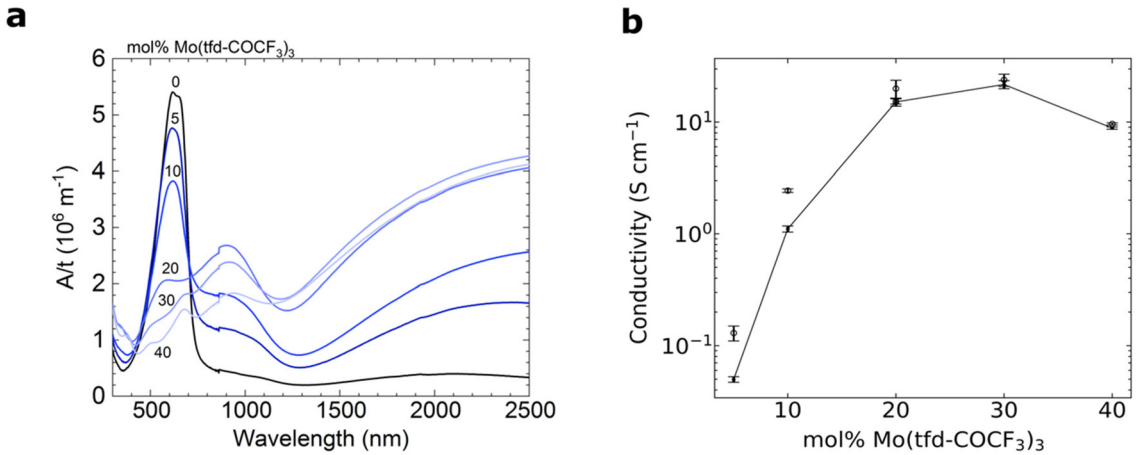

Fig. 5 (a) UV-Vis-NIR absorbance spectra with the measured absorbance *A* normalised by the film thickness *t*. (b) Electrical conductivity of 40–90 nm thick films of p($g_4$2T–T) doped with Mo(tfd-$COCF_3$)$_3$; average values and errors were obtained by measuring one sample for each dopant concentration five times and calculating the mean and standard deviation. The reproducibility of samples was confirmed by repeating the measurements on independently prepared films (Fig. S3† and open symbols in b).

of the number of nearby host sites and hence the dopants start to compete for host sites that they can ionise. This means that the dopants have a decreased probability of finding a host site that favours charge transfer, leading to a loss in ionisation efficiency. Note that this effect does not require large aggregated dopant phases, but the formation of clusters will likely lead to a further decrease of the ionisation efficiency. Moreover, electrostatic interactions between neighbouring mono- and/or dianions will be more severe when dopants form larger clusters, reducing the ability of every dopant to accept two electrons.

In light of the results from the current study, these recent reports offer reasonable explanations for the decreased conductivity at high concentrations of Mo(tfd-$COCF_3$)$_3$ dopant in p($g_4$2T–T). This indicates that even small clusters of dopants may have a detrimental impact on the electrical properties of the material and that the cluster morphology plays an important role.

Conclusions

The tomography method presented in this study yields insight with regard to the distribution of dopant clusters within organic semiconductor thin-films at sub-nanometre resolution. Specifically, utilising the *Z*-contrast from the dopant Mo(tfd-$COCF_3$)$_3$ mixed with the conjugated polymer p($g_4$2T–T), the 3D cluster nanostructure has been reconstructed, allowing the position of individual dopant species to be visualised. The usefulness of the technique is demonstrated by extracting quantitative information regarding cluster volume, aspect ratio and nearest-neighbour distance from the reconstructions. A heterogeneous distribution of dopant species is observed, with significantly longer average distances to neighbouring clusters compared to that of a hypothetical homogeneous distribution. Determining the position of dopant molecules at sub-nanometre resolution has the potential to improve the accuracy of transport models for doped organic semiconductors, since these models generally lack information regarding their fine-scale distribution of dopant species. The method presented here may also be utilised as a characterisation tool when designing dopant–organic semiconductor combinations in order to identify systems with minimal clustering. We note that the nature of dopant clusters is likely to vary considerably for different dopant and polymer combinations, for example, due to different tendencies of the neutral dopant to aggregate, different abilities of dopant ions to fit in the host structure with minimal disruption, and different extents of ionization arising from different IEs and EAs.

The reconstructed nanostructures show a growing cluster size and increasingly elongated cluster shape at higher dopant concentrations. Further, electrical measurements correlate changes in electrical conductivity with changes in dopant cluster size and shape. Despite this, the results show that the dopants remain sufficiently well dispersed to not be prevented from contact with the surrounding organic semiconductor matrix, indicating that the decreased conductivity is not due to formation of large dopant phases or a disruption of the organic semiconductor nanostructure. Instead, we suggest that the increased cluster size and change in size distribution observed in this study increase the energetic disorder. In addition, there is a lower number of neighbouring host sites that are available for electron transfer, which in turn leads to the decrease in electrical conductivity observed at high dopant concentrations. These results indicate that even clustering at the scale of only a few nanometres can have a significant impact on the electrical properties of the material, highlighting the need for characterisation techniques that offer a high degree of spatial resolution when developing doped organic semiconductors.

Author contributions

GP and EO conceived the study, performed the STEM and electron tomography experiments and analyses, contributed to the sample fabrication and wrote the manuscript. EJ contributed to the sample fabrication and performed the optical and electrical analysis. MR performed the quantitative data analysis. RK synthesised the polymer. YZ, SB and SM synthesised the dopant species.

Conflicts of interest

There are no conflicts of interest to declare.

Acknowledgements

We thank the Chalmers Material Analysis Laboratory for their support of the electron microscopes. We gratefully acknowledge financial support from the Swedish Research Council through grants 2016-06146 and 2018-03824 and from the National Science Foundation through the DMREF program (DMR-1729737).

References

1 B. Lüssem, M. Riede and K. Leo, *Phys. Status Solidi A*, 2013, **210**, 9–43.
2 R. M. Pankow and B. C. Thompson, *Polymer*, 2020, **207**, 122874.
3 W. Tress, *Organic Solar Cells Theory, Experiment, and Device Simulation*, Springer, Cham, Switzerland, 2014.
4 A. F. Paterson, S. Singh, K. J. Fallon, T. Hodsden, Y. Han, B. C. Schroeder, H. Bronstein, M. Heeney, I. McCulloch and T. D. Anthopoulos, *Adv. Mater.*, 2018, **30**, 1801079.
5 D. Champier, *Energy Convers. Manage.*, 2017, **140**, 167–181.
6 B. Russ, A. Glaudell, J. J. Urban, M. L. Chabinyc and R. A. Segalman, *Nat. Rev. Mater.*, 2016, **1**, 1–14.
7 P. Cheng, G. Li, X. Zhan and Y. Yang, *Nat. Photonics*, 2018, **12**, 131–142.
8 C. Li, J. Zhou, J. Song, J. Xu, H. Zhang, X. Zhang, J. Guo, L. Zhu, D. Wei, G. Han, J. Min, Y. Zhang, Z. Xie, Y. Yi, H. Yan, F. Gao, F. Liu and Y. Sun, *Nat. Energy*, 2021, **6**, 605–613.
9 S. Yuvaraja, A. Nawaz, Q. Liu, D. Dubal, S. G. Surya, K. N. Salama and P. Sonar, *Chem. Soc. Rev.*, 2020, **49**, 3423–3460.
10 I. Salzmann and G. Heimel, *J. Electron Spectrosc. Relat. Phenom.*, 2015, **204**, 208–222.
11 I. E. Jacobs and A. J. Moulé, *Adv. Mater.*, 2017, **29**, 1703063.
12 S. N. Patel, A. M. Glaudell, K. A. Peterson, E. M. Thomas, K. A. O'Hara, E. Lim and M. L. Chabinyc, *Sci. Adv.*, 2017, **3**, e1700434.
13 A. Hamidi-Sakr, L. Biniek, J.-L. Bantignies, D. Maurin, L. Herrmann, N. Leclerc, P. Lévêque, V. Vijayakumar, N. Zimmermann and M. Brinkmann, *Adv. Funct. Mater.*, 2017, **27**, 1700173.
14 I. E. Jacobs, E. W. Aasen, J. L. Oliveira, T. N. Fonseca, J. D. Roehling, J. Li, G. Zhang, M. P. Augustine, M. Mascal and A. J. Moulé, *J. Mater. Chem. C*, 2016, **4**, 3454–3466.
15 K. Kang, S. Watanabe, K. Broch, A. Sepe, A. Brown, I. Nasrallah, M. Nikolka, Z. Fei, M. Heeney, D. Matsumoto, K. Marumoto, H. Tanaka, S. Kuroda and H. Sirringhaus, *Nat. Mater.*, 2016, **15**, 896–902.
16 J. E. Cochran, M. J. N. Junk, A. M. Glaudell, P. L. Miller, J. S. Cowart, M. F. Toney, C. J. Hawker, B. F. Chmelka and M. L. Chabinyc, *Macromolecules*, 2014, **47**, 6836–6846.
17 F. Deschler, D. Riedel, A. Deák, B. Ecker, E. von Hauff and E. Da Como, *Synth. Met.*, 2015, **199**, 381–387.
18 B. Kuei, M. P. Aplan, J. H. Litofsky and E. D. Gomez, *Mater. Sci. Eng., R*, 2020, **139**, 100516.
19 J. Euvrard, A. Revaux, P.-A. Bayle, M. Bardet, D. Vuillaume and A. Kahn, *Org. Electron.*, 2018, **53**, 135–140.
20 C.-Y. Chang, B.-C. Tsai, Y.-C. Hsiao, M.-Z. Lin and H.-F. Meng, *Nano Energy*, 2019, **55**, 354–367.
21 A. L. Dixon, H. Vezin, T.-Q. Nguyen and G. N. M. Reddy, *Mater. Horiz.*, 2022, **9**, 981–990.
22 Y. Yamashita, J. Tsurumi, M. Ohno, R. Fujimoto, S. Kumagai, T. Kurosawa, T. Okamoto, J. Takeya and S. Watanabe, *Nature*, 2019, **572**, 634–638.
23 H. Abdalla, G. Zuo and M. Kemerink, *Phys. Rev. B*, 2017, **96**, 241202.
24 S. Wilken, T. Upreti, A. Melianas, S. Dahlström, G. Persson, E. Olsson, R. Österbacka and M. Kemerink, *Sol. RRL*, 2020, **4**, 2000029.
25 S. K. Mohapatra, Y. Zhang, B. Sandhu, M. S. Fonari, T. V. Timofeeva, S. R. Marder and S. Barlow, *Polyhedron*, 2016, **116**, 88–95.
26 S. Zokaei, R. Kroon, J. Gladisch, B. D. Paulsen, W. Sohn, A. I. Hofmann, G. Persson, A. Stamm, P.-O. Syrén, E. Olsson, J. Rivnay, E. Stavrinidou, A. Lund and C. Müller, *Adv. Sci.*, 2020, **8**, 2002778.
27 E. Järsvall, T. Biskup, Y. Zhang, R. Kroon, S. Barlow, S. R. Marder and C. Müller, *Chem. Mater.*, 2022, **34**, 5673–5679.
28 S. A. Paniagua, J. Baltazar, H. Sojoudi, S. K. Mohapatra, S. Zhang, C. L. Henderson, S. Graham, S. Barlow and S. R. Marder, *Mater. Horiz.*, 2014, **1**, 111–115.
29 R. Kroon, D. Kiefer, D. Stegerer, L. Yu, M. Sommer and C. Müller, *Adv. Mater.*, 2017, **29**, 1700930.
30 W. O. Saxton, W. Baumeister and M. Hahn, *Ultramicroscopy*, 1984, **13**, 57–70.
31 J. R. Kremer, D. N. Mastronarde and J. R. McIntosh, *J. Struct. Biol.*, 1996, **116**, 71–76.
32 J. M. LeBeau and S. Stemmer, *Ultramicroscopy*, 2008, **108**, 1653–1658.
33 D. Donhauser, M. Pfannmöller, L. Dieterle, K. Schultheiß, R. R. Schröder, W. Kowalsky and M. Kröger, *Adv. Funct. Mater.*, 2013, **23**, 2130–2136.
34 I. Salzmann, G. Heimel, M. Oehzelt, S. Winkler and N. Koch, *Acc. Chem. Res.*, 2016, **49**, 370–378.

35 I. Sahalianov, J. Hynynen, S. Barlow, S. R. Marder, C. Müller and I. Zozoulenko, *J. Phys. Chem. B*, 2020, **124**, 11280–11293.
36 V. Untilova, J. Hynynen, A. I. Hofmann, D. Scheunemann, Y. Zhang, S. Barlow, M. Kemerink, S. R. Marder, L. Biniek, C. Müller and M. Brinkmann, *Macromolecules*, 2020, **53**, 6314–6321.
37 C. J. Boyle, M. Upadhyaya, P. Wang, L. A. Renna, M. Lu-Díaz, S. P. Jeong, N. Hight-Huf, L. Korugic-Karasz, M. D. Barnes, Z. Aksamija and D. Venkataraman, *Nat. Commun.*, 2019, **10**, 1–10.
38 A. Fediai, A. Emering, F. Symalla and W. Wenzel, *Phys. Chem. Chem. Phys.*, 2020, **22**, 10256–10264.